# CHAPTER 6

## $Bi_2O_3$ Doped $SrFe_8Al_4O_{19}$ Series

### 6.1 Introduction

In the previous chapter, 24.44 kOe of $H_c$ is attained for the $SrFe_{7.98}Ni_{0.02}Al_4O_{19}$ composition, which is the highest ever $H_c$ in any rare-earth free magnet and even greater than $Nd_2Fe_{17}B$ (15.07 kOe) to a great extent. However, less $M_s$ (9.9 emu/g) is observed for that composition, which is required to improve for high energy density in the material. Hard magnets are the primary material for producing an isotropic/anisotropic permanent magnet. Higher values of both $M_s$ and $H_c$ are desirable for high $(BH)_{max}$, which can collectively result in a good permanent magnet. In $M_s$ increment, high bulk density also plays a dynamic role (Thakur et al., 2013b). High bulk density causes an increase in magnetic dipoles/unit volume and hence improves the $M_s$ value. It can be improved by controlling sintering characteristics and using different sintering aids such as glass, $Bi_2O_3$, $B_2O_3$, CuO, PbO, $SiO_2$, and $MoO_3$, which are liable for densifying mechanisms (Rahaman, 2017). So in the present chapter, $SrFe_8Al_4O_{19}$ is chosen as the base magnet to study further with the different concentrations of sintering aid and different sintering temperatures.

A composition of $SrFe_8Al_4O_{19}$_x$Bi_2O_3$ (x = 0, 1, 2, 3, 4, 5 wt%) is selected here to synthesize by the traditional solid-state reaction process. Based on the results of chapter 5, the 4 $Al^{3+}$ ion substitution in SrM magnet is further studied in this chapter. Bismuth oxide ($Bi_2O_3$) is reported as a good choice of sintering aid among various ferrites to improve the sintering behavior and magnetic properties (Long et al., 2017; Qiao et al., 2010; Su et al., 2005). Here, the effect of the different amounts of $Bi_2O_3$ (0-5 wt%) is analyzed to achieve better magnetic properties in the $SrFe_8Al_4O_{19}$ magnet. High $Bi_2O_3$ (>5 wt%) is avoided as

it may cause abnormal grain growth due to partial agglomeration since an inverse relationship is exhibited between grain growth rate and thickness of the liquid phase (LAY, 1968). It is a good ionic conductor and occupies places at the grain boundary, resulting in enhanced grain growth at a lower temperature due to the liquid phase formation. During the sintering process, the liquid phase forms at a high temperature as the melting point of $Bi_2O_3$ (825°C) is comparatively low (Liu et al., 2008). It promotes both grain size and bulk density with $Bi_2O_3$ doping concentration, which can help in the $M_s$ increment also. In this work, the effects of different sintering temperatures 850°C, 950°C, 1050°C, and 1150°C are also studied. For a low-temperature sintering process (< 900°C), it has been reported that the liquid phase of $Bi_2O_3$ can induce abnormal grain growth and modification in grain boundaries (Jeong et al., 2004). Also, higher temperatures over 1200°C can exaggerate grain growth such that some particles grow at a greater rate than their adjacent ones to a greater extent.

## 6.2 Results and Discussion

### 6.2.1 Analysis of $SrFe_8Al_4O_{19}$ Raw Powder

A TG/DTA curve of $SrFe_8Al_4O_{19}$ raw powder is shown in Fig. 6.1. It shows one exothermic and one endothermic peak in the DTA curve. An exothermic peak around 100-500°C shows complete evaporation of absorbed water, and the corresponding TG curve shows around 2% weight loss. An endothermic peak from 790-930°C is related to the decomposition of $SrCO_3$ into SrO and $CO_2$ and the reaction between SrO, $Al_2O_3$, and $Fe_2O_3$, which is resulted in the $SrAl_4Fe_8O_{19}$ formation, according to Eq. (6.1). An evident weight loss of ~28% is observed in this temperature range.

$$SrCO_3 \rightarrow SrO + CO_2 \uparrow \longrightarrow SrO + 4Fe_2O_3 + 2Al_2O_3 \longrightarrow SrAl_4Fe_8O_{19} \qquad (6.1)$$

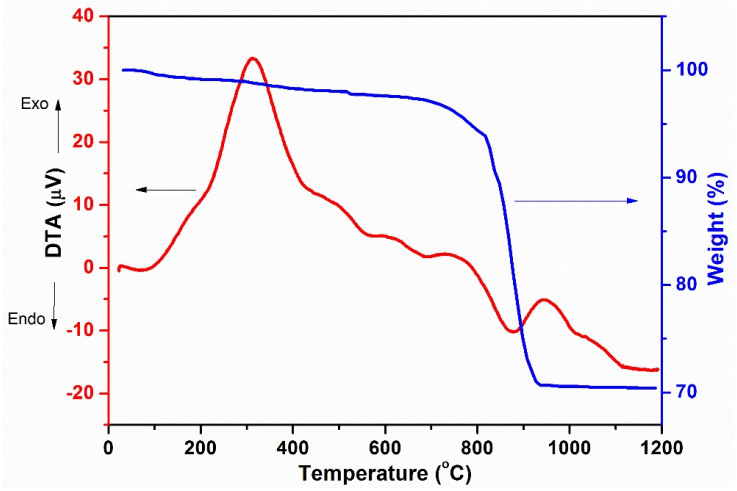


**Figure 6.1** *TG/DTA curve of $SrFe_8Al_4O_{19}$ raw powder.*

## 6.2.2 Analysis of $SrFe_8Al_4O_{19}$ Calcined Powder

The FTIR pattern of $SrFe_8Al_4O_{19}$ calcined powder in the frequency range of 4000-400 $cm^{-1}$ is shown in Fig. 6.2(a). Three characteristic peaks appear here, which belong to the stretching vibration of the Fe-O bond at lattice sites in the formation of hexaferrite (Torkian et al., 2016). The characteristic peaks that appeared at (444 $cm^{-1}$) and (576 $cm^{-1}$ & 622 $cm^{-1}$) are attributed to the ionic vibration at the octahedral site and tetrahedral site, respectively. These peaks are in the acceptable absorption band range reported for strontium hexaferrite and confirm the formation of a single-phase M-type structure (Xie et al., 2018).

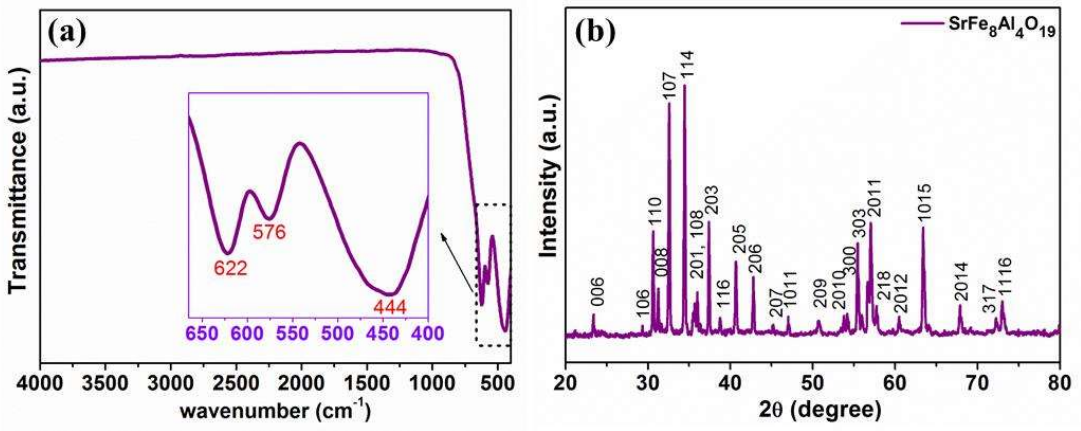


**Figure 6.2** *(a) FT-IR spectra and (b) XRD pattern of $SrFe_8Al_4O_{19}$ calcined powder.*

The XRD pattern of $SrFe_8Al_4O_{19}$ calcined powder is shown in Fig. 6.2(b). All the intense diffraction peaks are matched to the diffraction profile of $SrFe_{12}O_{19}$, ICDD card no. 79-1411 (Wang et al., 2012), having a space group of *$P6_3/mmc$*. The absence of any additional peak within the acceptable limit approves the phase formation of single-phase hexagonal structure and successful substitution of $Al^{3+}$ ions in the SrM structure. For the calcined $SrFe_8Al_4O_{19}$ powder, these values of structural parameters are observed as $a/b$ = 5.83 Å, $c$ = 22.82 Å, $V_{cell}$ = 671.71 Å$^3$, and $\chi D$ = 4.68 g/cm$^3$.

## 6.2.3 Analysis of $SrFe_8Al_4O_{19}$_x$Bi_2O_3$ ($0 \leq x \leq 5$ wt%) Sintered Pellets

### 6.2.3.1 Structural Properties

The XRD patterns of $SrFe_8Al_4O_{19}$_x$Bi_2O_3$ ($0 \leq x \leq 5$ wt%) pellets, sintered at 1050$^o$C, are shown in Fig. 6.3. The diffraction profile of all sintered pellets with the varying content of $Bi_2O_3$ has confirmed the phase formation of a single M-type hexaferrite structure. The prominent diffraction peaks are analogous to the XRD pattern of $SrFe_{12}O_{19}$ (ICDD card no. 79-1411) and are indexed accordingly. The structural parameters of $SrFe_8Al_4O_{19}$_x$Bi_2O_3$ ($0 \leq x \leq 5$ wt%) sintered pellets at 1050$^o$C are listed in Table 6.1. A minor change in lattice parameters '*a*' and '*c*' is observed in all the samples. It indicates the behavior of $Bi_2O_3$ as a sintering aid, where Bi ion does not occupy lattice sites of Fe (propensity to the tetragonal site); rather, it only contributes to the densification mechanism. A minor variation in lattice parameter '*c*' signifies the perpendicular direction possibility of (001) hexagonal face with the direction of applied pressure (Long et al., 2017). The value of the *c/a* ratio is observed in the range of 3.91-3.92. It indicates the formation of a magnetoplumbite hexagonal structure as its typical value is less than 3.98.

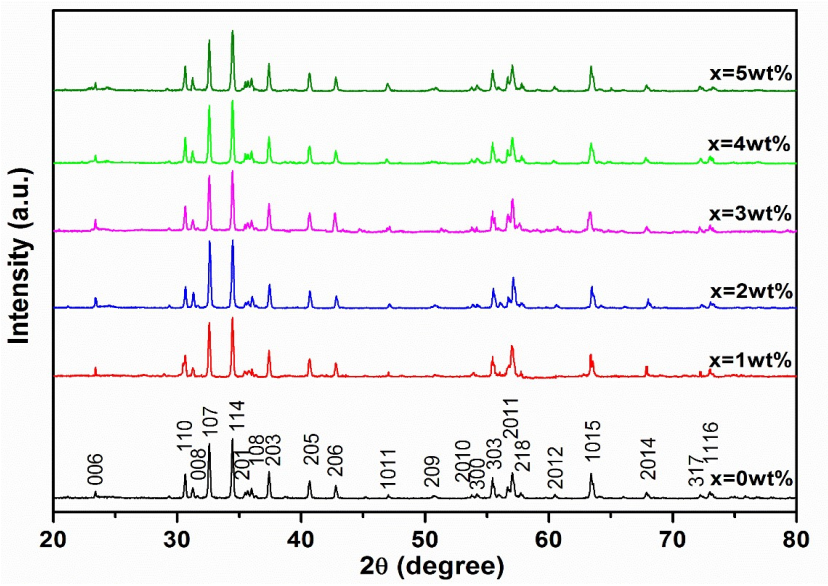


**Figure 6.3** *XRD pattern of $SrFe_8Al_4O_{19}$_$xBi_2O_3$ ($0 \leq x \leq 5$ wt%) hexaferrites sintered at 1050°C temperature.*

**Table 6.1** *Structural parameters of $SrFe_8Al_4O_{19}$_$xBi_2O_3$ ($0 \leq x \leq 5$ wt%) hexaferrites sintered at 1050°C temperature.*

| $Bi_2O_3$ (wt%) | Lattice Parameter | | *c/a* | *V* (Å$^3$) | *χD* (g/cm$^3$) | $G_{avg}$ (μm) |
|---|---|---|---|---|---|---|
| | *a, b* (Å) | *c* (Å) | | | | |
| 0 | 5.83 | 22.82 | 3.91 | 671.7 | 4.68 | 0.83 |
| 1 | 5.83 | 22.82 | 3.91 | 671.7 | 4.73 | 0.91 |
| 2 | 5.83 | 22.83 | 3.92 | 672.1 | 4.77 | 1.16 |
| 3 | 5.83 | 22.83 | 3.92 | 672.5 | 4.82 | 1.95 |
| 4 | 5.84 | 22.84 | 3.91 | 674.2 | 4.85 | 1.97 |
| 5 | 5.84 | 22.84 | 3.91 | 674.6 | 4.89 | 2.02 |

### 6.2.3.2 Densification and Microstructural Properties

The objective of this work is mainly focused on the improvement of magnetic characteristics, which likely depends on the densification mechanism. (Long et al., 2017) have observed that the $Bi_2O_3$ sintering aid of 2-4 wt% in strontium hexaferrite exhibits higher density with compact microstructure, resulting in improved magnetic properties of SrM. The bulk density (BD) of all the sintered samples for different content of sintering aid

$Bi_2O_3$ and at different sintering temperatures ($T_{sin}$) is given in Table 6.2. The increasing amount of $Bi_2O_3$ and increasing $T_{sin}$ are found to be favorable for density improvement. $Bi_2O_3$ is responsible for density improvement due to the liquid phase formation during the sintering process. It promotes the ion and vacancy transformation in and among the grains. Thus, it introduces the collective effect of driving force due to grain and grain boundaries, which helps in the sintering mechanism and results in dense samples (Wu et al., 2015).

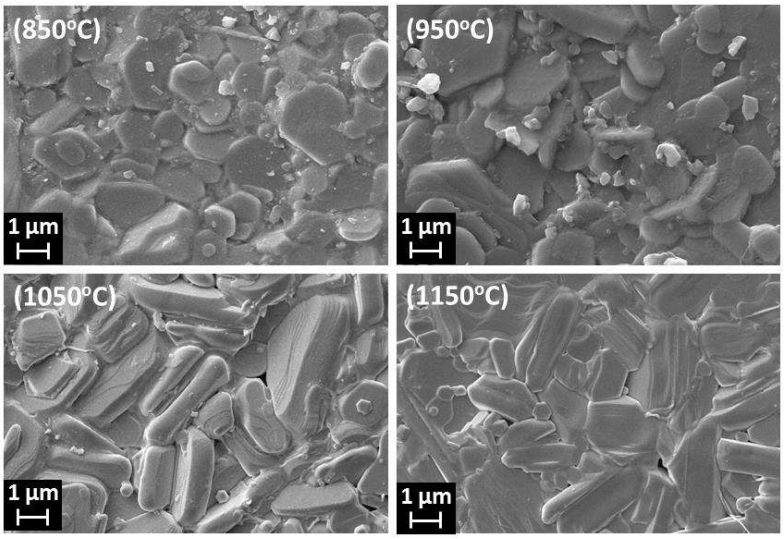


**Figure 6.4** *SEM images of $SrFe_8Al_4O_{19}$_$xBi_2O_3$ (x = 3 wt%) hexaferrite sintered at 850°C to 1150°C.*

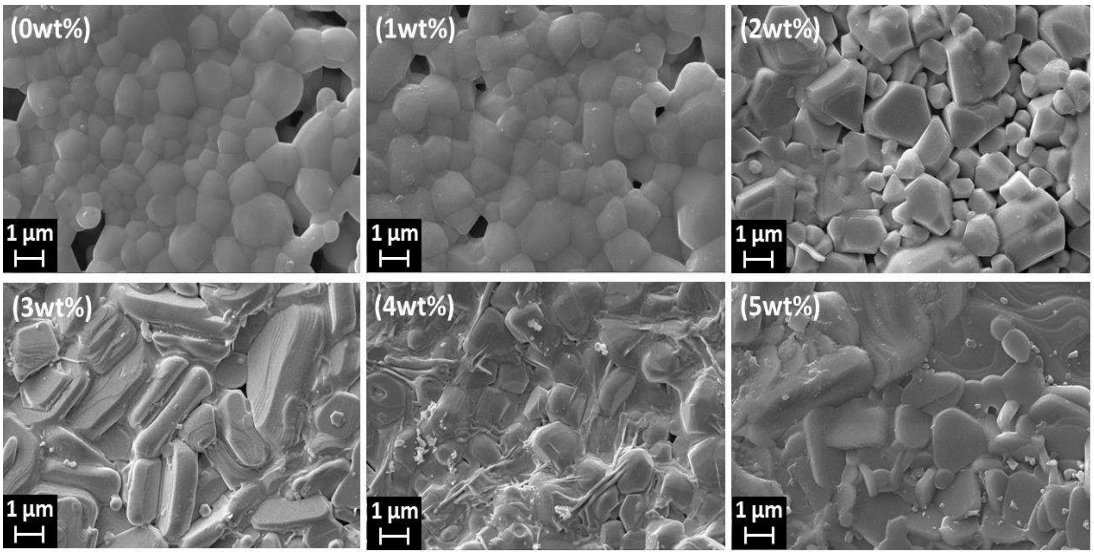


**Figure 6.5** *SEM images of $SrFe_8Al_4O_{19}$_$xBi_2O_3$ ($0 \leq x \leq 5$ wt%) hexaferrite sintered at 1050°C.*

SEM micrographs of $SrFe_8Al_4O_{19}$_x$Bi_2O_3$ (x = 3 wt%) pellets sintered at different sintering temperatures (850°C ≤ $T_{sin}$ ≤ 1150°C) are shown in Fig. 6.4. These micrographs confirm the formation of hexagonal platelet-like morphology in all samples. Their average grain sizes are found as 1.48 μm (850°C), 1.67 μm (950°C), 1.95 μm (1050°C), and 2.06 μm (1150°C). An increase in sintering temperature boosts the grain growth mechanism and increases the average grain size of the ceramics. Higher $T_{sin}$ causes the reduction of both step-free energy and critical driving force (Cao, 2004). Therefore, it results in more number of grains having the driving force for grain growth ($\Delta g$) more significant than the critical driving force ($\Delta g_C$), and promote grain growth in the system. SEM micrographs of $SrFe_8Al_4O_{19}$_x$Bi_2O_3$ (0 ≤ x ≤ 5 wt%) pellets sintered at 1050°C are shown in Fig. 6.5 to specify the effect of $Bi_2O_3$ in the microstructure of Al-substituted SrM magnets. These micrographs confirm the formation of hexagonal platelet-like morphology in all samples, and their average grain size is given in Table 6.1. With the increasing $Bi_2O_3$ content, an increase in grain size is observed. A low melting point of $Bi_2O_3$ promotes the effective rise in grain size due to the liquid-channel structure. The liquid channel causes a drop in friction between particles, leading to the rearrangement and the elimination of the solid-vapor interface in the samples. The effect of $Bi_2O_3$ is not dominantly sighted in the grains structure for x = 1 wt% compared to x = 0 wt%, though it improves the bulk density by eliminating pores. In the samples with x ≤ 1 wt%, significant grain growth is not observed, as none of the grains might have a higher driving force for grain growth ($\Delta g$) than the critical driving force ($\Delta g_C$) and so no rapid growth is observed (Vu et al., 2013). The samples with x ≥ 2 wt% display some large grains that have grown rapidly in a hexagonal structure of fine grains. When $Bi_2O_3$ content exceeds (x ≥ 2 wt%), it may promote diffusion across the grain boundaries resulting in lower step-free energy and lower critical driving force (Vu et al., 2013). So, in these samples, few grains might achieve $\Delta g > \Delta g_C$ and results in abnormal

grain growth of those grains until $\Delta g$ becomes lower than $\Delta g_C$. It consequently causes an increase in average grain size.

### 6.2.3.3 Magnetic Properties

Hysteresis curves of $SrFe_8Al_4O_{19}$_$xBi_2O_3$ ($0 \leq x \leq 5$ wt%) at different sintering temperatures of 850°C, 950°C, 1050°C, and 1150°C are shown in Fig. 6.6. The values of magnetic parameters are listed in Table 6.2 with different $Bi_2O_3$ content and at different $T_{sin}$. Variations in $M_s$ and $H_c$ of $SrFe_8Al_4O_{19}$_$xBi_2O_3$ ($0 \leq x \leq 5$ wt%) with different $Bi_2O_3$ content and $T_{sin}$ can be visualized in Fig. 6.7.

**Table 6.2** *Bulk density (BD), saturation magnetization ($M_s$), remanent magnetization ($M_r$), squareness ratio ($M_r/M_s$), and coercivity ($H_c$) of $SrFe_8Al_4O_{19}$_$xBi_2O_3$ ($0 \leq x \leq 5$ wt%) with different sintering temperatures (850 to 1150°C) at 300K.*

| $T_{sin}$ (°C) | $Bi_2O_3$ (wt%) | BD (gm/cm$^3$) | $M_s$ (emu/g) | $M_r$ (emu/g) | $M_r/M_s$ | $H_c$ (kOe) |
|---|---|---|---|---|---|---|
| 850 | 0 | 3.12 | 10.69 | 4.77 | 0.45 | 11.31 |
| | 1 | 3.19 | 11.82 | 5.30 | 0.45 | 11.56 |
| | 2 | 3.23 | 12.63 | 5.75 | 0.46 | 11.73 |
| | 3 | 3.34 | 13.45 | 5.98 | 0.44 | 11.10 |
| | 4 | 3.35 | 11.98 | 5.51 | 0.46 | 9.41 |
| | 5 | 3.45 | 12.97 | 5.81 | 0.45 | 7.28 |
| 950 | 0 | 3.24 | 12.02 | 5.39 | 0.45 | 11.97 |
| | 1 | 3.25 | 13.84 | 5.50 | 0.40 | 11.52 |
| | 2 | 3.36 | 14.28 | 6.68 | 0.47 | 9.99 |
| | 3 | 3.61 | 15.22 | 6.61 | 0.43 | 10.30 |
| | 4 | 3.62 | 12.89 | 5.64 | 0.44 | 7.52 |
| | 5 | 3.72 | 13.73 | 6.33 | 0.46 | 5.58 |
| 1050 | 0 | 3.40 | 13.82 | 6.38 | 0.46 | 9.49 |
| | 1 | 3.41 | 15.62 | 6.55 | 0.42 | 9.84 |
| | 2 | 3.76 | 15.73 | 6.61 | 0.42 | 9.64 |
| | 3 | 4.13 | 16.42 | 6.90 | 0.42 | 9.78 |
| | 4 | 4.14 | 14.27 | 6.25 | 0.44 | 7.54 |
| | 5 | 4.11 | 15.26 | 7.03 | 0.46 | 6.78 |
| 1150 | 0 | 3.41 | 12.02 | 5.45 | 0.45 | 12.42 |
| | 1 | 3.46 | 12.57 | 5.67 | 0.45 | 12.57 |
| | 2 | 4.17 | 12.41 | 5.58 | 0.45 | 12.74 |
| | 3 | 4.35 | 12.51 | 5.72 | 0.46 | 13.05 |
| | 4 | 4.43 | 12.13 | 5.50 | 0.45 | 10.41 |
| | 5 | 4.44 | 13.16 | 5.82 | 0.44 | 7.31 |

The $M_s$ values of all samples are in the range of 10.69-16.42 emu/g. A higher value of $M_s$ ~16.42 emu/g is found, which is higher than the previously reported values for the $SrFe_8Al_4O_{19}$ composition (Luo et al., 2012; Shekhawat & Roy, 2019; Torkian et al., 2016; Wang et al., 2012). $M_s$ parameter is mainly affected by site preference of substituted elements or resultant magnetic moment and magnetic collinearity. It is reported that the substitution of $Al^{3+}$ ion into the structure of M-type hexagonal ferrite has a preferential tendency to the lattice sites 12*k* and 2*a* (Wang et al., 2017). Due to the replacement of $4Fe^{3+}$ ($5\mu_B$) ions by $4Al^{3+}$ ($0\mu_B$) ions, both 12*k* (↑) and 2*a* (↑) sites are reasons for the reduction of net magnetic moment ($\mu_{net} = 0$) and hence results in a small $M_s$ value. Small $M_s$ value can also be explained by magnetic collinearity. Magnetic moments of Fe ions are collinearly arranged in $SrFe_{12}O_{19}$ because of superexchange interactions among Fe ions. When $Al^{3+}$ ions are substituted, the existing magnetic collinearity is broken down due to the suppressed superexchange interaction by non-magnetic ($0\mu_B$) $Al^{3+}$ ion (Liu et al., 2011). It results in the massive reduction of $M_s$ in Al-substituted SrM hexaferrite. With the increasing $Bi_2O_3$ content, $M_s$ value of all the samples increases till x = 3 wt% following a reduction on further increment in x. A decreasing pattern of both $M_s$ and $H_c$ in the ferrites is reported for higher $Bi_2O_3$ content (x > 3 wt%) (Long et al., 2017). $M_s$ value of all the samples increases till $T_{sin} \leq 1050^oC$ due to the densification mechanism. Further escalation in $T_{sin}$ results in the diminished value of $M_s$ because of weakening in exchange interaction by higher sintering temperature. Increasing $M_s$ may be attributed to the increase in bulk density and grain size. Improvement in bulk density causes a decrease in the demagnetizing field and increases the spin-rotational contribution, which may increase $M_s$. According to the variation in $M_s$, a related varying pattern in $M_r$ is observed for all the samples.

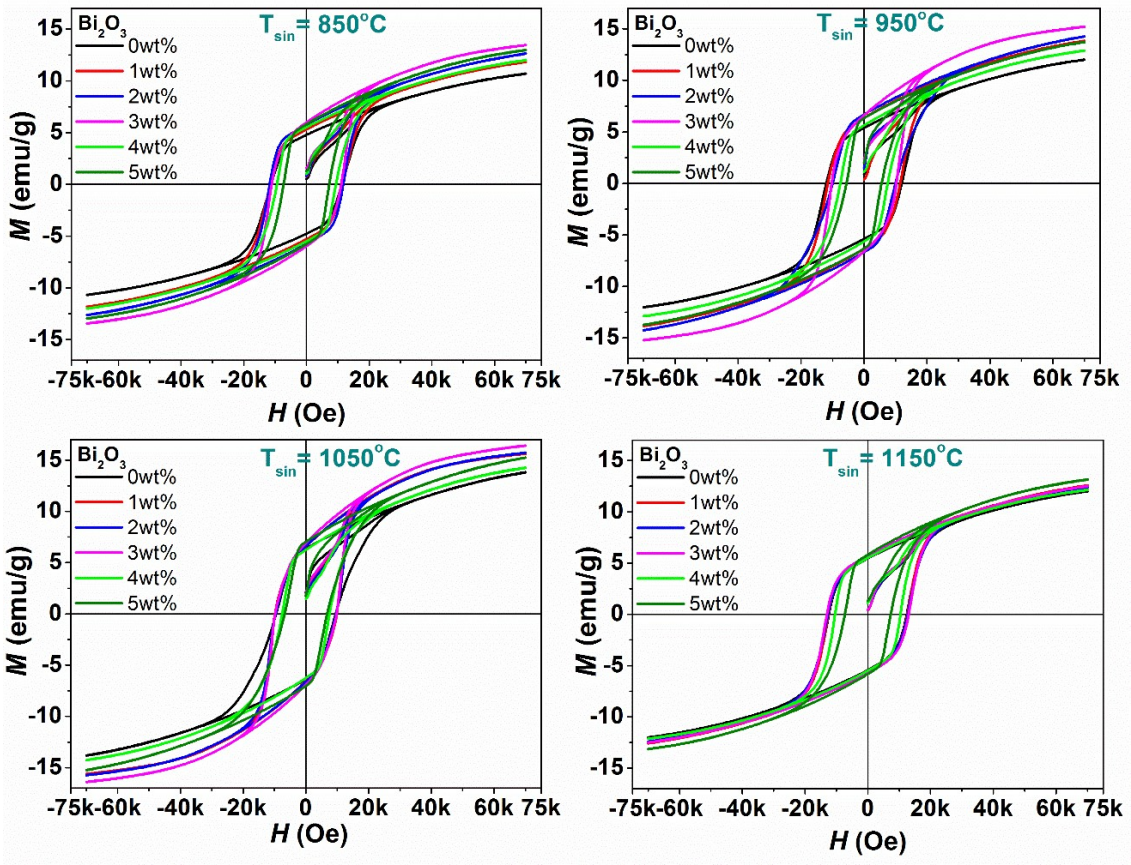


**Figure 6.6** *Hysteresis curve of $SrFe_8Al_4O_{19}$_$xBi_2O_3$ ($0 \leq x \leq 5$ wt%) hexaferrites sintered at 850°C-1150°C sintering temperature.*

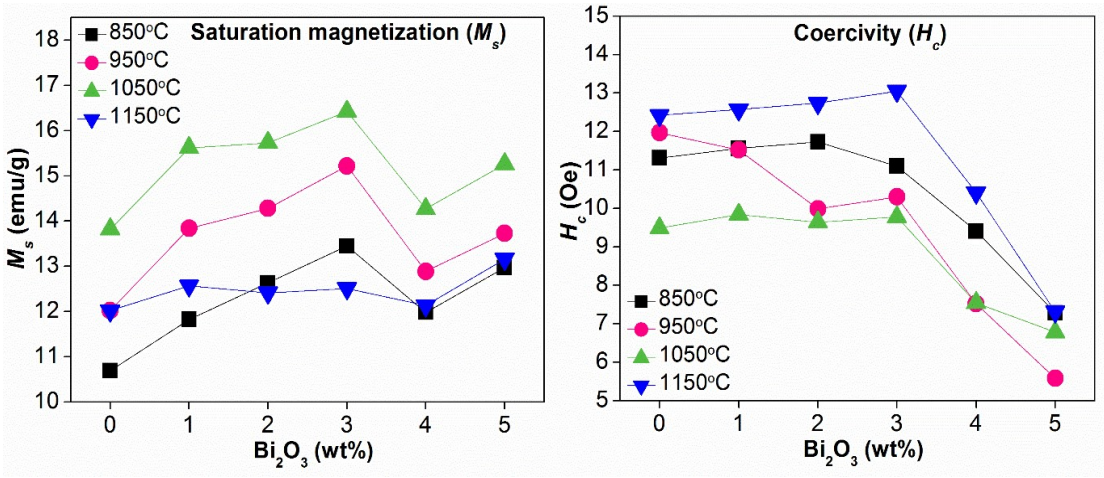


**Figure 6.7** *Variation in $M_s$ and $H_c$ of $SrFe_8Al_4O_{19}$_$xBi_2O_3$ ($0 \leq x \leq 5$ wt%) hexaferrites with different $Bi_2O_3$ content and sintering temperatures.*

The $H_c$ values are in the range of 5.58-13.05 kOe. Most samples have greater $H_c$ values than the maximum theoretical $H_c$ value of 7.5 kOe (Torkian et al., 2016) of SrM. A

higher $H_c$ of 13.05 kOe is obtained with $Bi_2O_3$ content of 3 wt%, sintered at 1150°C, which is less than the 18.1 kOe reported by (Luo et al., 2012) in $SrFe_8Al_4O_{19}$, though the $M_s$ value in the present work is improved by 39% than the (Luo et al., 2012) work. $H_c$ is observed to increase till x = 3 wt% for the samples sintered at $T_{sin}$ = 1150°C; it reduces drastically after that. The higher sintering temperature is reported as a favorable factor for $H_c$ enhancement in Al-contained Sr-hexaferrite (Chen et al., 2008). $Al^{3+}$ (0.51Å) substitution at $Fe^{3+}$ (0.64Å) leads to lattice distortion due to ionic radius difference. It introduces micro-stress in the system, which acts as the enhancing parameter of both coercivity and magnetocrystalline anisotropy (Wang et al., 2012). Higher sintering temperature causes the escalation in this stress, resulting in the enhancement of $H_c$ with an increase in $T_{sin}$. Theoretically, $H_c$ depends on many factors like particle size, substitution behavior of transition elements, structural morphology, density, and defects (Ram, 1990). The first two parameters play a prominent role in the $H_c$ trend. For the small content of sintering aids, the substitutional behavior of $Al^{3+}$ ion might be dominated and causes the $H_c$ enhancement.

The area confined under the loop indicates the total energy absorbed by the material during each cycle. The shape of these hysteresis loops has quantified the magnetic domain behavior of materials and is characterized by the squareness ratio ($M_r/M_s$). The square shape of hysteresis loop suggests a high degree of magnetic symmetry, i.e., the structure has as many directions as possible towards the easy magnetization direction. The concave curve shape indicates that wall pinning is a dominant factor in the coercivity mechanism that restricts the rotation of magnetization. The squareness ratio ($M_r/M_s$) is found to be less than 0.5 for all the samples, which indicates that samples are in the multi-domain region. In this region, coercivity became inversely proportional to the grain size. The increasing average grain size of samples due to the sintering aid dominantly effect and cause a reduction in $H_c$. The increasing tendency of average grain size indicates growth in grain demagnetization

factor while a reduction in grain size factor value (Du et al., 2020), resulting in $H_c$ reduction. Moreover, according to the Stoner-Wohlfarth model (Kazin et al., 2008), coercivity is indirectly proportional to saturation magnetization, which is the reason for the varying pattern of $H_c$. The eventual drop in the $M_s$ value of the samples sintered at 1150°C causes the $H_c$ tendency of these samples with the higher coercivity value.

### 6.2.3.4 Dielectric Properties

The dielectric constant ($\varepsilon$) and dielectric tangent loss ($tan\delta$) of $SrFe_8Al_4O_{19}$_x$Bi_2O_3$ ($0 \leq x \leq 5$ wt%) samples at different $T_{sin}$ are recorded with respect to the frequency and shown in Fig. 6.8 and Fig. 6.9, respectively. The values of $\varepsilon$ and $\tan\delta$ at 1 MHz frequency are comprehensively listed in Table 6.3.

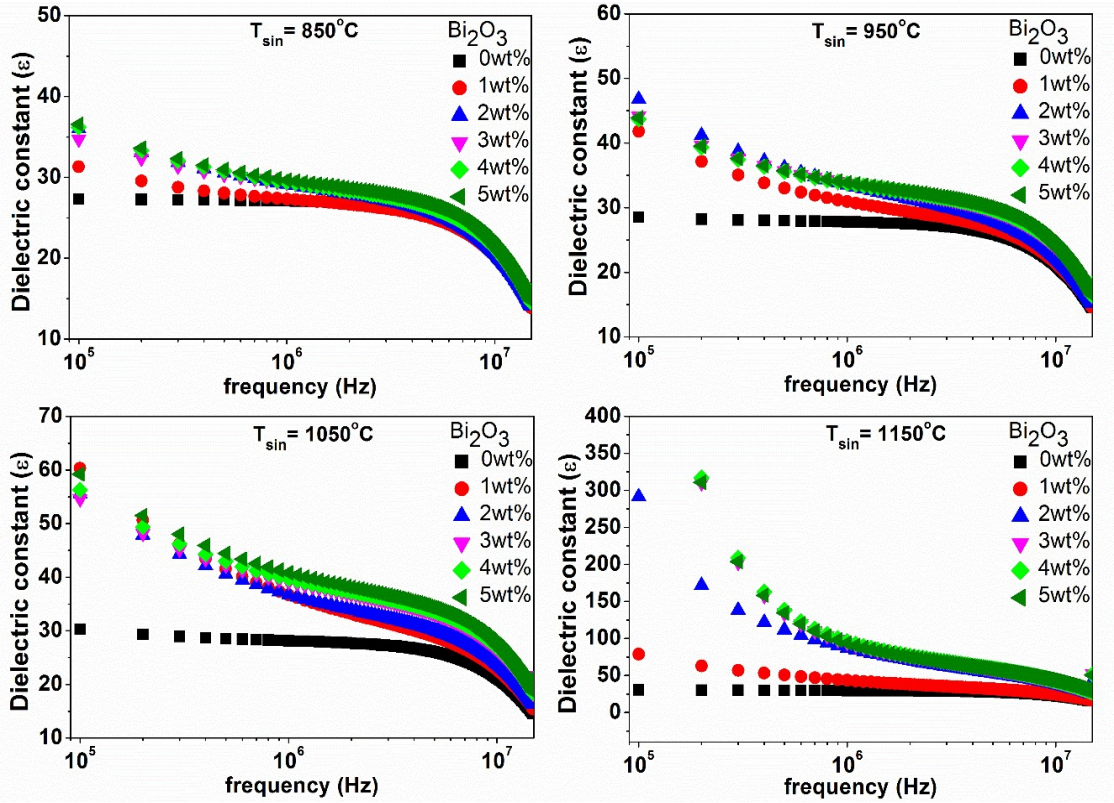


**Figure 6.8** *Frequency-dependent dielectric constant behavior of $SrFe_8Al_4O_{19}$_x$Bi_2O_3$ ($0 \leq x \leq 5$ wt%) hexaferrites with different $Bi_2O_3$ content and at different sintering temperatures.*

Analysis of dielectric constant and dielectric loss tangent is helpful in understanding the conduction mechanism and the behavior of electric charge carriers. The dispersion due to interfacial dipole polarization (Maxwell-Wagner model) and intrinsic dipole polarization (Koop model) mainly contributes to the dielectric properties of the hexaferrite (Praveena et al., 2015). According to Koop's model, the structure of hexaferrite comprises two layers: conducting grain layer and poor conducting grain boundaries. Due to the transfer of electrons among divalent and trivalent Fe ions, electron movement became limited in the applied field direction and resulted in polarization. A typical ferrite behavior of $\varepsilon$ is observed for all the samples, i.e., a decreasing pattern of $\varepsilon$, with increasing frequency (Shakoor et al., 2014). Such behavior is caused by the lagging of electron transfer between Fe ions behind the alternating applied field, which results in declining polarization with increasing frequency. The varying trend of $\varepsilon$ became nearly constant at higher frequencies (~1 MHz). At these frequencies, the conduction mechanism turns out to be insensitive to the frequency, and the polarization of induced moments can not synchronize with the frequency of the applied field.

A continuous increase in the dielectric constant is observed with both $Bi_2O_3$ content and sintering temperature. The introduction of Bi ion shows its effect at the tetrahedral site. It increases $Fe^{3+}$ ions and charge transfer between Fe ions at the octahedral site, which increases the charge polarization and results in the improvising $\varepsilon$ value (Shakoor et al., 2014). It may support the increasing $\varepsilon$ value with the increasing $Bi_2O_3$ content. In general, the dielectric constant exhibits a growing tendency with the increasing temperature, which is more evident in the lower frequency region (Auwal et al., 2016). As observed in Fig. 6.8, increasing sintering temperature results in a continuous increase of $\varepsilon$ value due to the thermal activation energy. Higher sintering temperatures encourage the densification process. A dielectric constant mainly depends on the density; higher the density higher

would be the value of $\varepsilon$. High density reduces the porosity in the sample, i.e., the reduction of trapped air having $\varepsilon$ value ~1, and hence an increasing trend in $\varepsilon$ value is observed in all the samples (Vinaykumar & Bera, 2019).

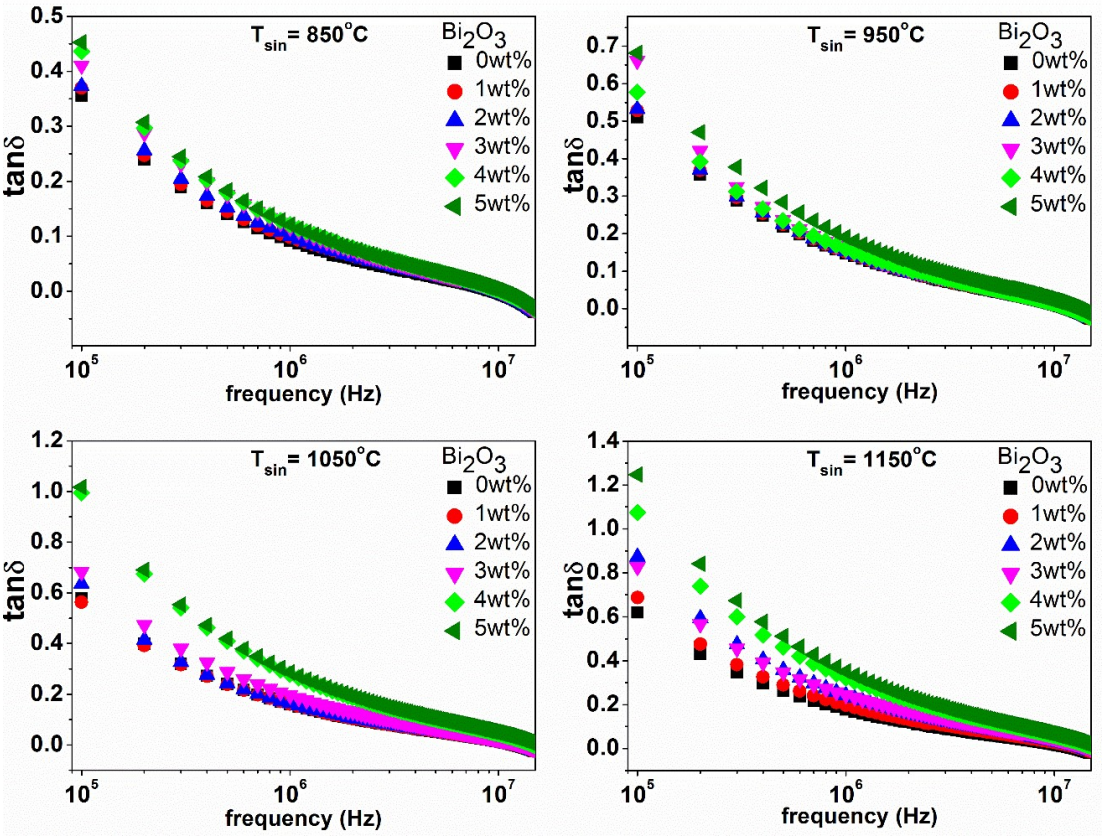


**Figure 6.9** *Frequency-dependent dielectric loss (tan$\delta$) of $SrFe_8Al_4O_{19}$_x$Bi_2O_3$ ($0 \leq x \leq 5$ wt%) hexaferrites with different $Bi_2O_3$ content and at different sintering temperatures.*

Dielectric tangent loss (*tan$\delta$*) has many origins, such as electron polarization loss, ionic vibration loss, ionic deformation loss, and ionic migration loss (Praveena et al., 2015). The most noteworthy contributor of *tan$\delta$* has resulted from the presence of two valance states of Fe ions that causes the switching of excess electrons among Fe ions, and the electronic conduction results in dielectric losses. Higher energy is required to switch these electrons among Fe ions at lower frequencies while it reduces with the increasing frequency, resulting in the decreasing trend of *tan$\delta$*, as shown in Fig. 6.9. Significant dipole interactions are also reduced with the increasing frequency, which is another factor for the

decaying pattern of *tanδ*. Increasing temperature causes increasing mobility of charge carriers, i.e., improvement in electrical conductivity and dielectric polarization. They collectively increase the value of tan$\delta$ with the increasing sintering temperature. Small *tanδ* is desirable for implementing magnetic material in different high-frequency applications.

**Table 6.3** *Dielectric constant (ε), dielectric loss (tanδ), ac-resistivity (ρ), and ac-conductivity (σ) of $SrFe_8Al_4O_{19}$_$xBi_2O_3$ ($0 \leq x \leq 5$ wt%) hexaferrite with different $Bi_2O_3$ content and at different sintering temperatures (850-1150°C) at 300K.*

| $T_{sin}$ (°C) | $Bi_2O_3$ (wt%) | $\varepsilon$ (at 1MHz) | $tan\delta$ (at 1MHz) | $\rho$ ($10^4$ Ω-cm) | $\sigma$ ($10^{-6}$ S-cm$^{-1}$) |
|---|---|---|---|---|---|
| 850 | **0** | 27.1 | 0.0923 | 71.86 | 1.39 |
| | **1** | 27.3 | 0.0979 | 67.25 | 1.49 |
| | **2** | 29.2 | 0.1007 | 61.13 | 1.64 |
| | **3** | 29.4 | 0.1164 | 52.52 | 1.90 |
| | **4** | 29.4 | 0.1207 | 50.65 | 1.97 |
| | **5** | 29.7 | 0.1209 | 50.06 | 2.00 |
| 950 | **0** | 27.8 | 0.1478 | 43.75 | 2.29 |
| | **1** | 30.9 | 0.1514 | 38.42 | 2.60 |
| | **2** | 33.5 | 0.1522 | 35.25 | 2.84 |
| | **3** | 33.8 | 0.1572 | 33.83 | 2.96 |
| | **4** | 33.7 | 0.1589 | 33.57 | 2.98 |
| | **5** | 33.9 | 0.1904 | 27.85 | 3.59 |
| 1050 | **0** | 28.1 | 0.1604 | 39.88 | 2.51 |
| | **1** | 36.7 | 0.1612 | 30.38 | 3.29 |
| | **2** | 36.8 | 0.1641 | 29.77 | 3.36 |
| | **3** | 39.2 | 0.1949 | 23.53 | 4.25 |
| | **4** | 39.7 | 0.2789 | 16.23 | 6.16 |
| | **5** | 40.8 | 0.2858 | 15.41 | 6.49 |
| 1150 | **0** | 29.5 | 0.1772 | 34.39 | 2.91 |
| | **1** | 43.4 | 0.1972 | 21.00 | 4.76 |
| | **2** | 87.4 | 0.2426 | 8.48 | 11.80 |
| | **3** | 94.3 | 0.2438 | 7.82 | 12.79 |
| | **4** | 96 | 0.3219 | 5.82 | 17.19 |
| | **5** | 3.7 | 0.3515 | 5.46 | 18.32 |

## 6.2.3.5 Electrical Properties

The fluctuating behavior of ac-resistivity ($\rho$) of $SrFe_8Al_4O_{19}$_$xBi_2O_3$ ($0 \leq x \leq 5$ wt%) samples with different $Bi_2O_3$ content and at different $T_{sin}$ is shown in Fig. 6.10. A similar

kind of variation pattern is observed for all the samples. The room-temperature values of both ac-resistivity ($\rho$) and ac-conductivity ($\sigma$) at 1 MHz frequency are listed in Table 6.3.

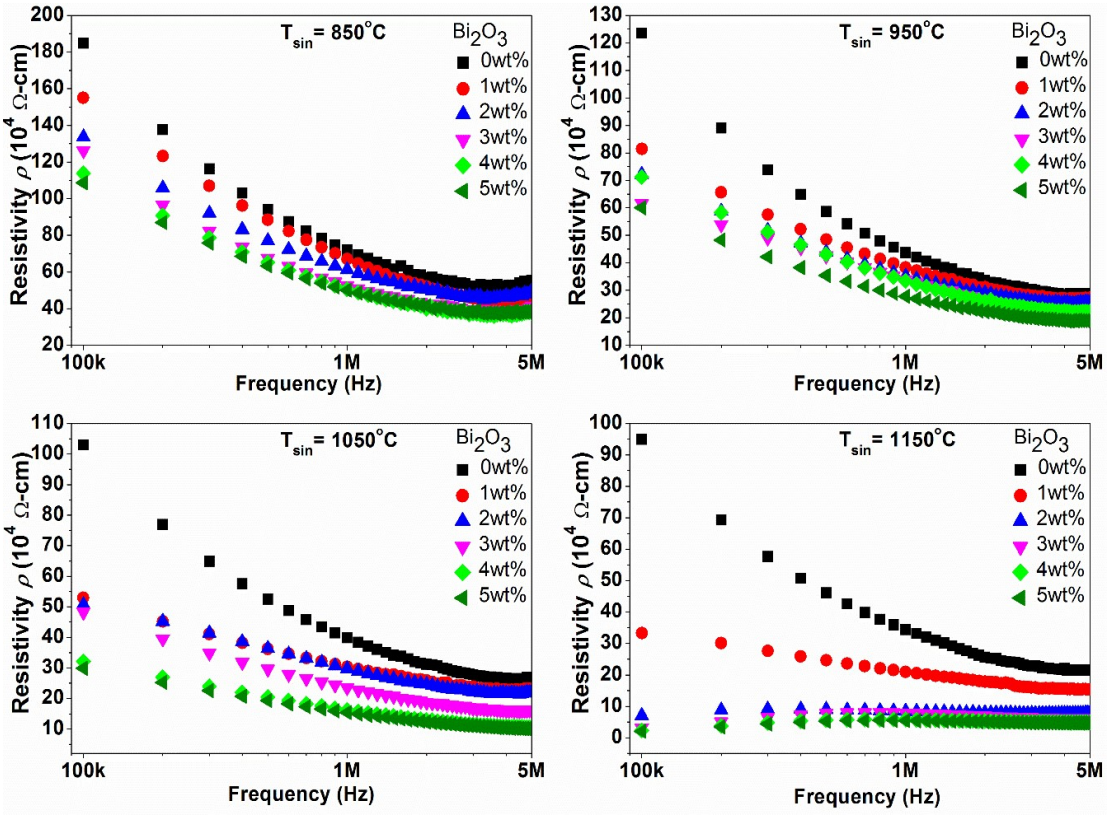


**Figure 6.10** *Frequency-dependent ac resistivity of $SrFe_8Al_4O_{19}$_$xBi_2O_3$ ($0 \leq x \leq 5$ wt%) hexaferrites with different $Bi_2O_3$ content and at different sintering temperatures.*

A higher $\rho$ value of hexagonal ferrite is required for complete penetration of high-frequency waves and to minimize eddy current losses at higher frequencies. It is desirable for most applications. Generally, $\rho$ decreases with the frequency according to the Maxwell-Wagner model and Koop model. The substitution of Al ions in the SrM hexaferrite tends to occupy the octahedral site of Fe ions. Hence, Al ions replace the $Fe^{3+}$ and result in the increase of $Fe^{2+}$ ions at the octahedral site. It eventually increases the hopping phenomenon and causes a decrease in resistivity with increasing frequency. According to the structural model of Maxwell-Wagner and Koop theory (conducting grain and poor conducting grain boundary), grains become active in the higher frequency region. They promote the

conduction phenomenon and result in the decreasing pattern of $\rho$. Both $Bi_2O_3$ content and $T_{sin}$ are found to decrease the resistivity value. Such behavior is caused by increasing grain size with increasing $Bi_2O_3$ content and $T_{sin,}$ as described in the microstructural analysis. Large grains promote the conduction mechanism of charge carriers and result in the diminishing value of $\rho$.

The ac-conductivity of hexaferrite depends on the hopping phenomenon of electrons between Fe ions of octahedral and tetrahedral sites. With the increasing frequency, electrons gain at least the threshold hopping energy required to switch from one site to another and cause an increase in conductivity (Ahmad et al., 2016). Variation in $\sigma$ obeys Jonscher's power law (Sekulic et al., 2015) as given by Eq (6.2)

$$\sigma_{ac} = Pw^n \tag{6.2}$$

where $P$ is the ac-coefficient that defines the polarizability strength, and n is known as frequency exponent confines as $0 \leq n \leq 1$. If $n = 0$, it means that electrical conduction is frequency independent, whereas, for $n \leq 1$, electrical conduction becomes frequency-dependent due to the relaxation phenomenon raised by the motion of mobile charge carriers (Thansanga et al., 2020). According to Jonscher, when these carriers move from their original place to the newer one, they stay in the moving state between two potential energy minima. Typically, $\sigma$ is an increasing parameter with frequency if caused by the hopping mechanism, while it is a decreasing parameter with frequency if it results from band conduction (Hashim et al., 2012). In the lower frequency region, the conduction mechanism is predominantly governed by the grain boundaries (region of energy state mismatch between adjacent grains), acting as the electron movement barrier. It causes lower conductivity and, subsequently, higher resistivity in the lower frequency region. With increasing frequency, grains become highly active and promote the hopping mechanism of

electrons between Fe ions according to the Verwey de Boer conduction mechanism (Sekulic et al., 2015). It results in an increasing pattern of $\sigma$ in the high frequency region.

## 6.3 Conclusions

Hexagonal ferrites are an essential component of electrical devices. These magnets can support the shifting of operating frequency to the higher ranges as per the requisite due to technological advancement. A composition of $SrFe_8Al_4O_{19}$_$xBi_2O_3$ ($0 \leq x \leq 5$ wt%) is successfully synthesized by solid-state reaction process. Structural, magnetic, and dielectric properties are studied to see the effect of $Bi_2O_3$ sintering aid and different sintering temperatures on the characteristic properties of the $SrFe_8Al_4O_{19}$ hexaferrite. A 3 wt% of $Bi_2O_3$ doping is optimized here to realize a higher value of $M_s$ ~16.42 emu/g in $SrFe_8Al_4O_{19}$ with the sintering temperature of 1050$^o$C, which is higher than the previously reported values for the $SrFe_8Al_4O_{19}$ (Luo et al., 2012; Shekhawat & Roy, 2019; Torkian et al., 2016; Wang et al., 2012). A high $H_c$ value of ~13.05 kOe is found for 3 wt% $Bi_2O_3$ doping at 1150$^o$C sintering temperature, which is less than the 18.1 kOe reported by (Luo et al., 2012) in $SrFe_8Al_4O_{19}$, though the $M_s$ value in the present work is improved by 39% than (Luo et al., 2012) work. All the synthesized samples show high resistive values, which correspondingly cause low eddy current losses. It assures that SrM-based magnets can be used in permanent magnet applications and can also withstand higher currents without significant performance degradation in PM applications.